BNL-216281-2020-JAAM

Strain Stabilized Nickel hydroxide Nanoribbons for Efficient Water Splitting

X. P. Wang, Y. Du

To be published in "ENERGY & ENVIRONMENTAL SCIENCE"

November 2020

Photon Sciences

Brookhaven National Laboratory

U.S. Department of Energy

USDOE Office of Science (SC), Basic Energy Sciences (BES) (SC-22)

DISCLAIMER

Strain Stabilized Nickel hydroxide Nanoribbons for Efficient Water Splitting

Authors: X. P. Wang[1#], H. J. Wu[1#], S. B. Xi[2], W. S. V. Lee[1,] J. Zhang[3], Z. H. Wu[3], J. O. Wang[3], T. D. Hu[3], L. M. Liu[4], Y. Han[4], S. W. Chee[5], S. C. Ning,[1] U. Mirsaidov[6], Z. B. Wang[7], Y.W. Zhang[8], A. Borgna[2], J. Wang[1], Y. H. Du[2,9,*], Z. G. Yu[7*], S. J. Pennycook[1*] and J. M. Xue[1*]

Affiliations:

[1] Department of Materials Science and Engineering, National University of Singapore, Singapore, 117575.

[2] Institute of Chemical and Engineering Sciences, Agency for Science, Technology and Research, Singapore, 627833.

[3] Beijing Synchrotron Radiation Facility, Institute of High Energy Physics, Chinese Academy of Sciences, Beijing 100049, People's Republic of China.

[4] Advanced Membranes and Porous Materials Center, Physical Science and Engineering Division, King Abdullah University of Science and Technology, Thuwal 23955-6900, Saudi Arabia.

[5] Centre for Bioimaging Sciences, 14 Science Drive 4, National University of Singapore, Singapore 117557, Singapore.

[6] Department of Physics, National University of Singapore, Singapore 117551, Singapore.

[7] School of Chemistry and Chemical Engineering, Harbin Institute of Technology, Heilongjiang Sheng 150006, China.

[8] Institute of High Performance Computing, Agency for Science, Technology and Research, Singapore, 138632.

[9] Brookhaven National Laboratory, Bldg. 743, Upton, NY USA

# Equal contribution.

*Correspondence to: msexuejm@nus.edu.sg (J.M. Xue); steve.pennycook@nus.edu.sg (S.J. Pennycook); yuzg@ihpc.a-star.edu.sg (Z.G. Yu); du_yonghua@ices.a-star.edu.sg (Y.H. Du).

Abstract: Development of efficient and durable oxygen evolution reaction (OER) catalysts has a direct impact on water splitting efficiency and cost effectiveness. In this work, we report the successful synthesis of a new $Ni(OH)_2$ structure, strain-stabilized $Ni(OH)_2$ nanoribbons (NR-$Ni(OH)_2$) two to three layers thick, with widths of 2-5 nm, via an electro-oxidation route. Conventional $Ni(OH)_2$ usually has negligible OER activity, while NR-$Ni(OH)_2$ shows a high activity for the oxygen evolution reaction, an overpotential of 162 millivolts and furthermore exhibits long-term stability in alkaline electrolyte. The substantial reduction in overpotential of NR-$Ni(OH)_2$ is due to its easier OOH* adsorption by the active four-coordinated Ni edge sites. The enhanced catalytic activity of NR-$Ni(OH)_2$ makes it an excellent candidate for industrial applications.

Electrochemical water splitting to generate hydrogen is an indispensable technology for energy conversion and storage which can mitigate intermittency issues associated with wind and sunlight (*1*, *2*). However, in order to realize its practical potential, it is highly necessary to address the sluggish four electron-proton coupled oxygen-evolution reaction (*3*). Thus, demand for efficient and durable OER catalysts is surging as a strategy to enhance the water splitting efficiency which inevitably leading to better cost effectiveness (*4*). This demand eventually leads to substantial research effort in the development of various non-noble OER catalysts, including earth-abundant first-row (3d) transition-metal oxides (*5*), sulfides (*6*), selenides (*7*), phosphides (*8*), layered double hydroxides (*9*), metal-organic frameworks (MOFs) (*10*) and the newly developed perovskites (*11*, *12*).

Among these materials, $Ni(OH)_2$ is considered to be one of the most widely investigated OER catalytic materials due to the promising OER performance and cost-effectiveness. To further enhance the OER performance of $Ni(OH)_2$, some of the strategies including morphology and size control to increase the number of accessible active sites (*13*), and cation doping to enhance the OER activity of Ni sites (*14-16*) have yielded reasonable OER catalytic performances. Despite these significant efforts in morphology/size control and cation doping, the OER activity of $Ni(OH)_2$ remains to be less-than-satisfactory for an efficient OER catalyst. Thus, in order to achieve substantial improvement in OER activity of $Ni(OH)_2$, it is therefore necessary to consider the factors that could influence the material's intrinsic OER performance. To gain an insight on the performance of traditional $Ni(OH)_2$, DFT simulation on Gibbs free energy of OOH* adsorption (which is considered the rate determining step) for traditional $Ni(OH)_2$ based on full coordinated Ni atoms with 6 OH^- was performed, and it was calculated to be 0.62 V (Overpotential). Motivated by this finding, it is hypothesized that intrinsic OER properties of $Ni(OH)_2$ could be controlled via the reduction of this Gibbs free energy of OOH* adsorption through manipulating the Ni coordination number. Interestingly, by reducing Ni coordination to 4, such overpotential was drastically reduced to 0.36 V. This simulation result indicates higher OER activity can be achieved via a non-stochiometric partial Ni 4-coordinated in $Ni(OH)_2$ due to this lowering of Gibbs free energy of OOH* adsorption.

Despite the possibility of enhancing the intrinsic OER properties of $Ni(OH)_2$ via the presence of 4-coordinated Ni, there remains a tremendous challenge in stabilizing a non-stochiometric $Ni(OH)_2$ with 4 coordinated Ni with no such report is available to date (*17*). Such scarcity in stabilized partial Ni 4-coordinated $Ni(OH)_2$ significantly amplifies the urgency of such material as efficient OER catalyst. Thus, in this work, we report the first stabilized non-stochiometric $Ni(OH)_2$ nanoribbons with alternating 4- and 6- coordinated Ni edge atoms (NR-$Ni(OH)_2$), as an efficient OER catalyst. Such unique structure was realized through the introduction of tensile strain along the length direction of NR-$Ni(OH)_2$ (*18, 19*). With the presence of the 4-coordinated Ni, a new OER mechanism was identified and coupled with the lowering of Gibbs free energy of OOH* adsorption. As a result, an unprecedented OER performance with an overpotential of 162 mV at 10 mA/cm^2 was recorded. Theoretical calculations were employed which indicate the excellent OER activity was due to the presence of four-coordinated Ni sites, which could greatly decrease the energy for OOH^* adsorption (overpotential decrease from 0.62 to 0.36V). We believe we have presented a shifting paradigm in this pioneering work and such work will become a crucial strategy for future development of $Ni(OH)_2$ as OER catalyst.

The sample was synthesized through electro-oxidation of NiS_2 (more details are given in the Supplementary Materials). X-ray diffraction (XRD), transmission electron microscopy (TEM) and X-ray photoelectron spectroscopy (XPS) analyses of NiS_2 are shown in Figs. S4-5. The electro-oxidation process of NiS_2 was monitored using *operando* XAFS under chronopotentiometry (CP) at a fixed current of 10 mA cm^{-2}, revealing the phase transition from NiS_2 to $Ni(OH)_2$ and then to NiOOH (Figs. S6-12). The $Ni(OH)_2$ sample was finally obtained through the ethanol reduction of NiOOH, on the basis of the following reaction equation: Ni^{3+} + CH_3CH_2OH = Ni^{2+} CH_3CHO (*20*) (Fig. S7). The SEM images of Ni, NiS_2 and $Ni(OH)_2$ were shown in Fig. S13. It was observed that the particle size was increased slightly when Ni became NiS_2 upon sulfurization. The particle morphology was greatly changed when NiS_2 was transformed into $Ni(OH)_2$ upon electro-oxidation.

The sample was first examined using electron microscopy techniques in order to understand its nanostructure. Since $Ni(OH)_2$ is highly electron beam sensitive, different approaches to reduce the electron beam dose were taken. Figures 1(a, b) are low-magnification scanning transmission electron microscopy (STEM)-HAADF (high-angle annular dark field) and ABF (annular bright field) images showing a high density of needle-like nanostructures embedded in a carbon matrix. To reveal the detailed structure of these needle-like nanostructures, simultaneously acquired STEM-HAADF and ABF images with atomic resolution were made with a smaller probe size (lower current density) to avoid beam damage [Fig. 1(c)]. A high density of double [insets in Fig. 1(d)] and triple [Fig. 1(f1, f2)] layers with lengths of 10 to 20 nm are clearly observed. The interlayer spacing of the layers is ~0.47 nm, well matching the (001) plane spacing of β-$Ni(OH)_2$. In some places, several double layers align together with a separation of 0.67 nm, which reflects a weak bond between them, as shown in Fig. 1(d, e), while there is no such alignment for triple layers, as shown in Fig. S14 (c1, c2). A plane view of the layered structures can also be seen, with a lattice spacing of 0.23 nm, which corresponds to the (111) plane of NiO, as shown in Fig. 1(g). The presence of NiO is due to the de-oxyhydrogenation of $Ni(OH)_2$ (Detailed analysis is given in Fig. S15). Similar nanoribbon structures were also observed using low-dose TEM with a direct-detection camera (Fig. S16), and with the sample cooled to liquid nitrogen temperature (Fig. S17).

The composition of the nanostructures was analyzed using energy dispersive x-ray spectroscopy (EDS) and electron energy loss spectroscopy (EELS) on the aberration-corrected STEM, both showing that the sample only contains Ni and O (Figs. S18-19). The width of the layers could be semi-quantitively identified through combining sample thickness measurement by the EELS log-ratio method and EELS composition analysis, as shown in Fig. S20-21, suggesting that the layer width is 2-5 nm. To further identify these structural features, STEM image simulation was performed, using a supercell with one double-layer NR-$Ni(OH)_2$ (length: ~5.5 nm; width: ~4.1 nm) embedded within a carbon matrix (thickness: 50 and 60 nm), as shown in Fig. 1(h). Since the layers are unlikely to be aligned exactly along the [010] direction (Fig. 1(i)), a simulated STEM HAADF image for 5^o tilted layers was simulated, as shown in Fig. 1(j), which is comparable to the experimental observation. More details of the simulated STEM images are shown in Fig. S22.

Following the local structure identification, the sample was analyzed using synchrotron radiation-XRD, as presented in Fig. 1(k). Three diffraction peaks are observed in the range from 30^o to 70^o (2θ), including one asymmetric peak centered around 34^o, a wide shoulder from 35 to 42^o, and a relatively intense peak at 59.8^o. By comparing against the standard β-$Ni(OH)_2$ (PDF #14-0117), the asymmetric peak is ascribed to the (100) plane, which can be further resolved into two sub peaks at 33.6^o and 34.9^o, respectively (inset of Fig. 1k, Fig. S23e). The splitting of the (100) peak suggests that the three equivalent (100) lattice spacings are no longer the same (Fig. S24), which could be caused by distortion within the (001) plane of the sample. The shoulder can be further resolved into a broad peak centered at 39^o, which is ascribed to the (101) plane, suggesting that the sample is not single-layered (Fig. S25). The peak at 59.8^o matches the (110) plane well. However, the diffraction peak from the (001) planar stacking of β-$Ni(OH)_2$ is missing, suggesting that the sample has very few stacked layers, which is consistent with the STEM observation.

From the quantitative composition analysis and image simulation, coupled with the observation of the layered structure and nanoribbons using the low dose STEM, TEM and synchrotron radiation (SR)-XRD, it can be concluded that the $Ni(OH)_2$ has a two-dimensional nanoribbon structure, 10-20 nm in length, 2-5 nm in width and two or three layers in thickness, denoted as NR-$Ni(OH)_2$, as illustrated in Fig. 1(l). The structure of NR-$Ni(OH)_2$ was further studied using density functional theory (DFT) simulation. The most stable (001) plane structure of the nanoribbon is obtained by cutting along the direction with alternating O and Ni atoms (armchair edge) with the symmetric edge terminated by OH, as shown in Fig. 1 (m). (detailed DFT calculations can be found in the Supplementary Materials). It is revealed in the simulated structure that the edge consists of alternating four- and six-coordinated Ni atoms in a periodic manner. The four-coordinated Ni atom possesses 2 three-coordinated OH and 2 two-coordinated OH, leaving two dangling bonds available, while the six-coordinated Ni atom has 4 three-coordinated OH and 2 two-coordinated OH.

The $Ni(OH)_2$ sample was further examined using Ni *K*-edge X-ray absorption fine structure (XAFS), being benchmarked against conventional β-$Ni(OH)_2$. Fig. S23 a, c and d show X-ray absorption near edge structure (XANES) analysis and FT data of the EXAFS. The XANES and FT data are quite close to those of β-$Ni(OH)_2$, implying they have very similar local chemical environment. However, some mismatch exists between the sample and β-$Ni(OH)_2$: The absorption edge of the sample is red shifted by ~0.50 eV (Inset of Fig. S23a) and its Ni-O bond length is around 0.03 Å shorter (Fig. S23 c and d) as compared to β-$Ni(OH)_2$ (More detailed structure information are shown in Table S1). The red shift in the adsorption edge indicates, the Ni in NR-$Ni(OH)_2$ has a lower average valence than that in β-$Ni(OH)_2$, which is lower than two. This is in accord well with DFT simulation model, that the armchair edges in NR-$Ni(OH)_2$ are fully consisted of periodically unsaturated Ni, which would result in the decrease of average Ni valence (Fig. 1m). The lattice contraction within NR-$Ni(OH)_2$ was further studied, by comparing with the β-$Ni(OH)_2$ and NR-$Ni(OH)_2$ relaxed model. It shows that the obvious lattice contraction exists in the width direction especially at the edge, while only little contraction could be seen along the length direction.

It is noted that in the relaxed NR-$Ni(OH)_2$ model, the (100) plane spacing d_1 slightly increases along the nanoribbon length direction, which is no longer identical to the other two equivalent plane spacings d_2 and d_3 (Fig. S23f). This explains the splitting of the (100) diffraction peak observed in our SR-XRD studies (Fig. 1k). This indicated that there was an oriented lattice distortion within the (001) plane of the sample. Combining XAFS, DFT calculations and SR-XRD, we could conclude that there is a tensile strain along the length direction in NR-$Ni(OH)_2$, which stabilize the four-coordinated Ni in NR-$Ni(OH)_2$.

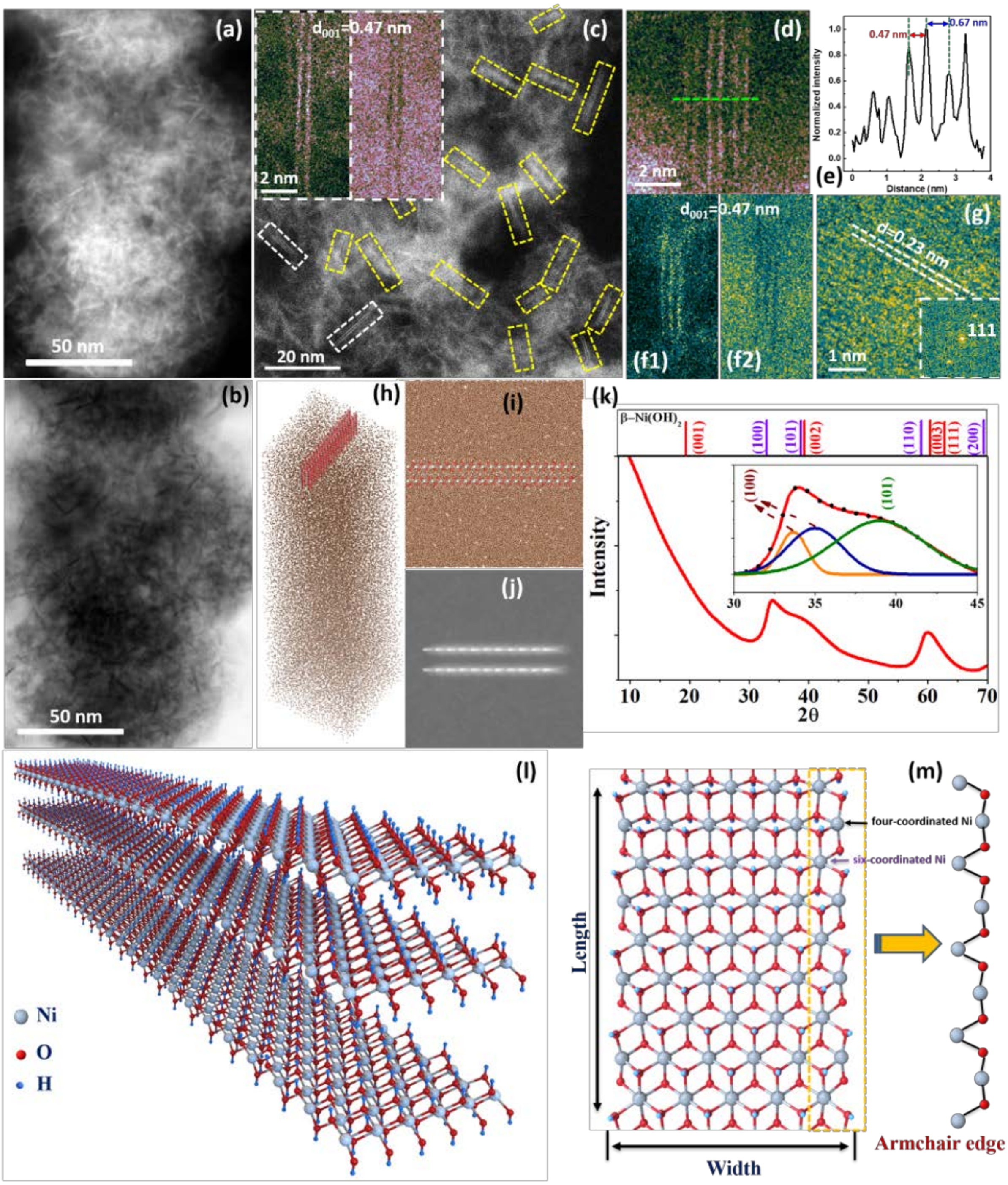

Fig. 1. Structural identification of NR-Ni(OH)₂. (a) Low-magnification STEM HAADF and (b) ABF image showing a high density of needlelike nanostructures embedded in the carbon matrix. (c) Atomically-resolved STEM HAADF image with low electron dose showing double and triple layers, some are marked with yellow dashed rectangular boxes, with enlarged HAADF and ABF images focusing on one double layer inset. (d) Enlarged STEM HAADF image showing a batch of double layers, aligning together. (e) Intensity profile along the line marked in (d). (f1, f2) Enlarged HAADF and ABF images focusing on one triple layer. (g) Enlarged STEM HAADF image showing the plan-view structure, with its FFT image inset. (h) Simulated structure model of one double-layer NR-Ni(OH)$_2$ (length: ~5.5 nm; width: ~4.1 nm) embedded in a carbon matrix (thickness: 50

nm). (i) View of layers from the top, exactly along [010] (layer plane). (j) Simulated STEM HAADF image, 5^{o} tilted away from the zone axis. (k) Synchrotron X-ray diffraction (SR-XRD) (Inset: SR-XRD fitting results in the angle range of 30-44^{o}). (l) (m) Simulated NR-$Ni(OH)_2$ structure.

The OER activity of NR-$Ni(OH)_2$ is evaluated in alkaline media (1 M KOH), using a three-electrode system. Conventional β-$Ni(OH)_2$ and pristine carbon cloth are used as controls. The morphology of β-$Ni(OH)_2$ on carbon cloth was provided in Fig. S26a. All reference electrodes were calibrated vs reversible hydrogen electrode (RHE) (Fig.S27). Polarization curves are measured from linear sweep voltammetry (LSV) (Fig. 2a), with 90% *iR* correction (Fig. S28). The pristine carbon paper shows almost zero activity. The NR-$Ni(OH)_2$ sample exhibits a much higher current density than β-$Ni(OH)_2$. Impressively, it only requires an overpotential of 162 mV to reach 10 mA cm^{-2}, which is nearly 150 mV lower than that of β-$Ni(OH)_2$. The corresponding Tafel slope of the NR-$Ni(OH)_2$ is 72 mV dec^{-1}, lower than that of β-$Ni(OH)_2$ (90 mV dec^{-1}), as shown in Fig. S29.

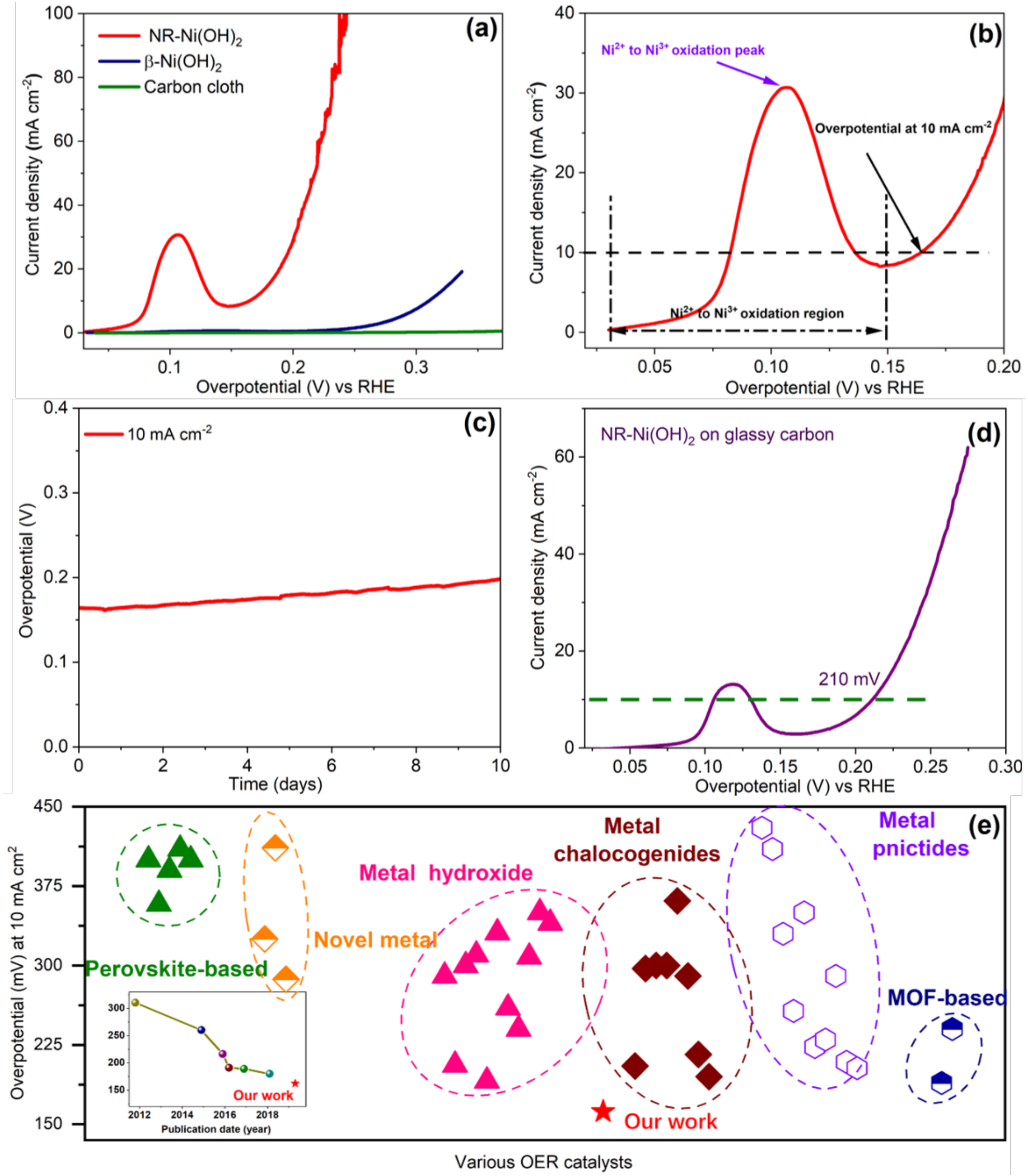

Fig. 2. Catalytic activity of NR-Ni(OH)$_2$ in 1M KOH solution. (a) OER polarization curves, with 0.1 mV s^{-1} scan rate and 90% *iR* correction (b) Magnified OER polarization curve for NR-Ni(OH)$_2$ catalyst; (c) chronopotentiometric curve at a constant current density of 10 mA cm^{-2}; (d) OER polarization curves of NR-Ni(OH)$_2$ on glassy carbon, with 0.1 mV s^{-1} scan rate and 90% *iR* correction; (e) Overpotential of NR-Ni(OH)$_2$ benchmarking against the reported catalysts (Inset: Chronological trend in overpotential of OER catalyst) (detailed reference seen in supporting information).

It is noted that the overpotential (162 mV) at 10 mA cm^{-2} is near to the nickel redox peak (120 mV), in Fig. 2b. Although a very slow scan rate (0.1 mV/s) was applied during LSV, it was very difficult to completely exclude the effect of nickel redox. In this work, the electro-oxidation process of NiS_2 was monitored using *operando* XAFS under chronopotentiometry (CP) at a fixed current of 10 mA cm^{-2} (detailed discussion could be seen in Fig. S6-12). Combining with the results of CP measurement and *operando* XAFS, it could be confirmed that the oxidation reaction from $Ni(OH)_2$ to NiOOH had been completed below the overpotential of 162 mV, suggesting that the current (10 mA cm^{-2}) at the overpotential of 162 mV is purely contributed from oxygen evolution. At the same time, we also conducted CV measurement with the scan rate of 0.1 mV/s (Fig. S30b). It could be seen that the overpotential at 10 mA cm^{-2} was 172 mV in both the positive and negative scans. By considering the (1.1 ohm) ohmic compensation, the overpotential value is around 161 mV, which is nearly the same as that of the LSV measurement. To the best of our knowledge, the overpotential of 162 mV at 10 mA cm^{-2} represents one of the best OER performance so far achieved, seen Fig. 2e (the points are detailed listed in Tables S2-4). To ensure the reliability of OER activity, five more NR-$Ni(OH)_2$ samples were prepared and tested (detailed information can be seen in Fig. S30c), with overpotentials ranging from 158 to 165 mV at 10 mA cm^{-2}, and an average of 162 mV. Furthermore, it shows excellent long-term stability, with an overpotential below 200 mV at 10 mA cm^{-2} after 10 days of operation (Fig. 2c).

The OER catalytic property are greatly influenced by the exposed surface areas of the catalyst, which are determined by catalyst loading mass, particle size/morphology of the catalyst, and the real substrate surface area (in particular for the porous substrate) (*13*). To exclude the surface area contribution from the porous carbon cloth, we also did the OER performance test on the flat electrode (glassy carbon, 0.3 mg cm^{-2}), as shown in Fig. 2d. The achieved overpotential at 10 mA/cm^2 was 210 mV, which is still one of the best as compared to other works using the same glassy carbon electrode, as listed in Tables S2 to 4.

In order to study the intrinsic active site activities of NR-$Ni(OH)_2$, the electrochemical active surface area (ECSA), normalized current density, and turnover frequencies (TOF) *etc* are provided were provided in Fig. 3. ECSA (cm^2) was calculated from the following equation: C_{DL}/C_s (C_{DL} (double layer capacitance) was the value calculated in Fig. 3c, and C_s value was 0.04). The current density normalized to their ECSA was presented in Fig. 3d, demonstrating that the intrinsic active site activity of NR-$Ni(OH)_2$ was much higher than that of the conventional β-$Ni(OH)_2$. The corresponding Tafel slopes, of which the current densities are normalized to their ECSAs, were presented in Fig. 3e, respectively. It is obvious that the Tafel slopes of NR-$Ni(OH)_2$ were lower than those of β-$Ni(OH)_2$. TOF was calculated through the following equation: TOF=$\frac{I}{4*F*n}$ (I: current in amperes; F: Faraday constant; n: number of moles of the active catalyst). Note, in this work all the catalysts were assumed to be active. The loading mass of NR-$Ni(OH)_2$ was 1.868 mg cm^{-2}, and β-$Ni(OH)_2$ was 0.701 mg cm^{-2}, which were worked out from ICP results. On the basis of the TOF results, it is obvious that the intrinsic active site activity of NR-$Ni(OH)_2$ was much better than that of the conventional β-$Ni(OH)_2$ (Fig. 3f).

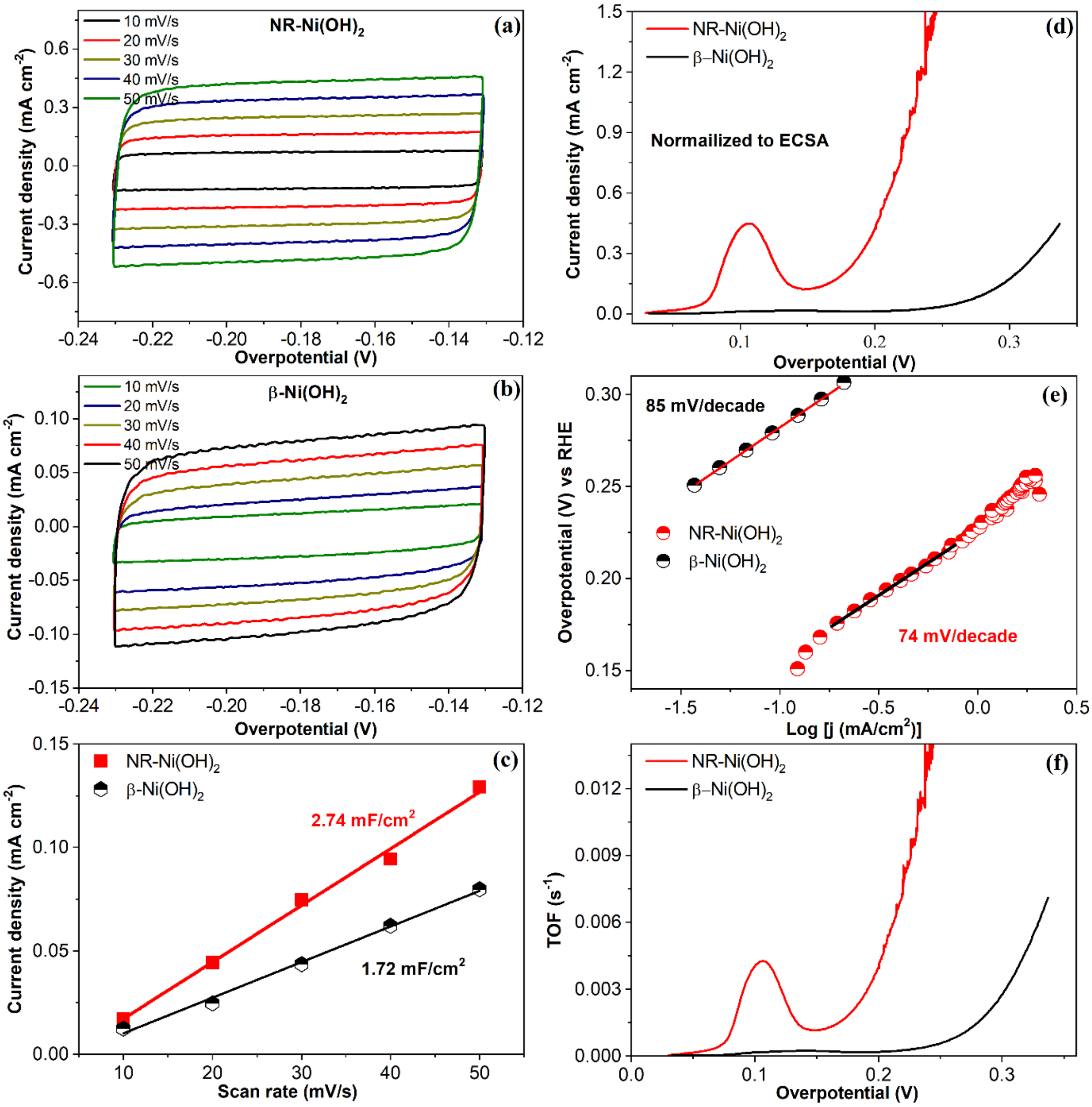

Fig. 3. The intrinsic catalytic of NR-Ni(OH)$_2$ in 1M KOH solution. (a)-(c) The electrochemical active area (ECSA) of NR-Ni(OH)$_2$ and β-Ni(OH)$_2$; (d) current density normalized to ECSA; (e) Tafel slop of NR-Ni(OH)$_2$ and β-Ni(OH)$_2$ when normalized to ECSA; (f) The turnover frequencies (TOF) of NR-Ni(OH)$_2$ and β-Ni(OH)$_2$.

It has been well known that β-Ni(OH)$_2$ would incidentally take up Fe ion from ubiquitous sources in aqueous KOH under anodic potential (*21, 22*) and Fe ion will enhance the OER activity performance of Ni(OH)$_2$ (*22*). To understand whether there is any Fe contamination in NR-Ni(OH)$_2$, the sample was analyzed using both EDS and STEM-EELS, showing that the sample only contains Ni and O (Figs. S18-19). The sample after OER measurement was further analyzed using STEM-EDS and inductively coupled plasma (ICP) chemical analysis. The EDS maps presented a uniform distribution of Ni and O over a wide view with no Fe detected, within the detection limit of 0.1 wt% (Fig. S31). The ICP result shows that Fe content in the sample was as low as 0.003%, of which the effect on OER activity could be ignored (Fig. S32).

Density functional theory (DFT) calculations were then carried out to understand the mechanism for the excellent catalytic properties of NR-Ni(OH)$_2$. In *operando* XAFS measurement, it is suggested that NR-Ni(OH)$_2$ is oxidized into NR-NiOOH first and thus NR-NiOOH would be the real active OER catalyst, which is also confirmed from the Ni $L_{2,3}$ edge X-ray absorption spectroscopy in Fig. S12. The XANES spectra indicated the Ni valence of NR-NiOOH was less than 3 (Fig. S7b) (*23*), which are different from the previous reported OER mechanism that Ni^{4+} sites are responsible for the OER process (*24-25*). In the 10 days operation measurement no structure changes were observed, which indicated NR-NiOOH has excellent stability (Fig. S31). Through the calculation of edge energies for different NR-NiOOH types (detailed calculation is provided in Supplementary Materials), the most stable edge configuration is used for OER simulation. Three kinds of active sites could be seen in the NR-NiOOH structure, including four- coordinated Ni and six-coordinated Ni at edge and Ni in the plane, as seen in the Fig. 4a. The OH^- absorption was the first step of the OER process, and it has been widely used as a main descriptor for OER activity trend (*4*). On the basis of DFT calculations, it is found that the four-coordinated Ni at the edge has the lowest OH^- adsorption energy, while the six-coordinated Ni at the edge and plane have the approximate value. The low absorption energy at the four coordinated Ni atoms was due to their more positive charge states, compared to other Ni atoms based on Bader charge analysis (Fig. 4b). Thus, in the OER process, the OH* species will be preferentially adsorbed onto the four coordinated Ni atoms at the edge. To further study the OER mechanism of NR-$Ni(OH)_2$, four steps including OH*, O*, OOH* absorption and O_2 release are considered, and the step 3 (OOH* adsorption process) is found to be the rate determining step, as shown in Fig. 4 (c-d) (*26-31*). Impressively, the calculated overpotential is only 0.362V, which is much lower than the reported β-NiOOH value 0.62V, in Table S5 (*28*). The high activity of NR-NiOOH is primarily due to its much easier OOH* adsorption process as compared to conventional β-$Ni(OH)_2$. Due to the abundant four-coordinated Ni atoms of the nanoribbon structure, NR-$Ni(OH)_2$ has a much improved OER activity than conventional β-$Ni(OH)_2$ in which the OER activity mainly relies on the basal plane Ni atoms.

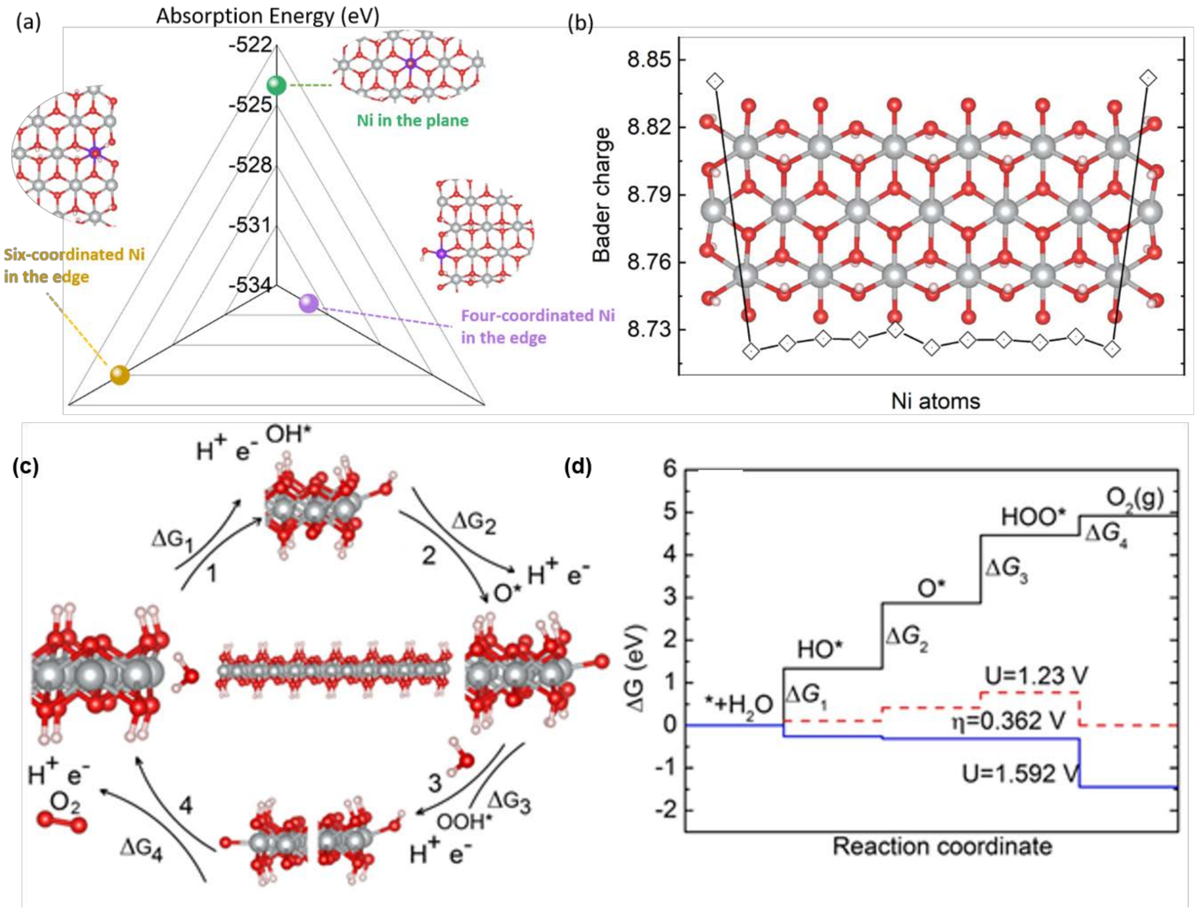

Fig. 4. OER mechanism. (a) The calculated OH^- absorption energy at different sites; (b) the Bader charge analysis; (c) Schematic of the four step OER mechanism of NR-$Ni(OH)_2$; (d) Calculated reaction free energy changes during the OER at U= 0, 1.23, and 1.592 V, denoted by the black, dashed red and solid blue lines, respectively.

In summary, we have synthesized an efficient and durable OER catalyst with remarkable activity, an overpotential of 162 millivolts at 10 milliamperes per square centimeter, and long-term stability in alkaline electrolyte. The structure best fits a strain stabilized double/triple layer nickel hydroxide nanoribbon structure, 2-5nm in width and 10-20 nm in length, and the four-coordinated Ni atoms in the edges are responsible for the OER activity.

References and Notes:

1. Luo, J., J. Mayer, Im, M. T., Schreier, M., Nazeeruddin, M. K., Park, N., Tilley, S. D., Fan, H. J., Gratzel, M. Water photolysis at 12.3% efficiency via perovskite photovoltaics and Earth-abundant catalysts. *Science* **345,** 1593-1596 (2014).
2. Cox, C. R., Lee, J. Z., Nocera, D. G., Buonassisi, T. Ten-percent solar-to-fuel conversion with nonprecious materials. *Proc. Natl. Acad. Sci. U.S.A.* **111,** 14057-14601 (2014).
3. Jiao, Y., Zheng, Y., Jaroniec, M., Qiao, S. Design of electrocatalysts for oxygen-and hydrogen-involving energy conversion reactions. *Chem. Soc. Rev.* **44,** 2060-2086 (2015).
4. Seh, Z. W., Kibsgaard, J., Dickens, C. F., Chorkendorff, I., Nørskov, J. K., Jaramillo, T. F. Combining theory and experiment in electrocatalysis: Insight into materials design. *Science* **355,** eaad4998 (2017).
5. Liang, Y., Li, Y., Wang, H., Zhou, J., Wang, J., Regier, T., Dai, H. Co_3O_4 nanocrystals on graphene as a synergistic catalyst for Oxygen Reduction Reaction. *Nat. Mater.* **10,** 780-786 (2011).
6. Zhu, H., Zhang, J., Yanzhang, R., Du, M., Wang, Q., Gao, G., Wu, J., Wu, G., Zhang, M., Liu, B., Yao, J., Zhang, X. When cubic cobalt sulfide meets layered molybdenum disulfide: a core-shell system toward synergetic electrocatalytic water splitting. *Adv. Mater.* **27,** 4752-4759 (2015).
7. Xu, X., Song, F., Hu, X. A nickel iron diselenide-derived efficient oxygen-evolution catalyst. *Nat. Commun.* **7,** 12324 (2016).
8. Hu, F., Zhu, S., Chen, S., Li, Y., Ma, L., Wu, T., Zhang, Y., Wang, C., Liu, C., Yang, X., Song, L., Yang, X., Xiong, Y. Amorphous metallic NiFeP: a conductive bulk material achieving high activity for oxygen evolution reaction in both alkaline and acidic media. *Adv. Mater.* **29,** 1606570 (2017).
9. Gong, M., Li, Y., Wang, H., Liang, Y., Wu, J. Z., Zhou, J., Wang, J., Regier, T., Wei, F., Dai, H. An advanced Ni-Fe layered double hydroxide electrocatalyst for water oxidation. *J. Am. Chem. Soc.* **135,** 8452-8455 (2013).

10. Zhao, S., Wang, Y., Dong, J., He, C., Yin, H., An, P., Zhao, K., Zhang, X., Gao, C., Zhang, L., Lv, J., Wang, J., Khattak, A. M., Khan, N. A., Wei, Z., Zhang, J., Liu, S., Zhao, H., Tang, Z. Ultrathin metal-organic framework nanosheets for electrocatalytic oxygen evolution. *Nat. Ener.* **1,** 16184 (2016).

11. Suntivich, J., May, K. J., Gasteiger, H. A., Goodenough, J. B., Shao-Horn, Y. A perovskite oxide optimized for oxygen evolution catalysis from molecular orbital principles. *Science* **334,** 6061 (2011).

12. Grimaud, A., Diaz-Morales, O., Han, B., Hong, W. T., Lee, Y., Giordano, L., Stoerzinger, K. A., Koper, M. M., Shao-Horn, Y. Activating lattice oxygen redox reactions in metal oxides to catalyze oxygen evolution. *Nat. Chem.* **9,** 457-465 (2017).

13. Luan, C., Liu, G., Liu, Y., Yu, L., Wang, Y., Xiao, Y., Qiao, Y., Dai, X., Zhang, X. Structure effects of 2D materials on α-Nickel hydroxide for oxygen evolution reaction. *ACS Nano*. **12,** 3875-3885 (2018).

14. Suen, N., Hung, S., Quan, Q., Zhang, N., Xu, Y., Chen, H. M. Electrocatalysis for the oxygen evolution reaction: recent development and future perspective. *Chem. Soc. Rev.* **46,** 337 (2017).

15. Huang, Z., Song, J., Du, Y., Xi, S., Dou, S., Nsanzimana, J., Wang, C., Xu, Z., Wang, X. Chemical and structural origin of the lattice oxygen oxidation in Co-Zn oxyhydroxide oxygen evolution electrocatalysts. *Nat. Ener.* **4,** 329-338 (2019).

16. Wang, J., Gan, L., Zhang, W., Peng, Y., Yu, H., Yan, Q., Xia, X., Wang, X. In situ formation of molecular Ni-Fe active sites on heteroatom-doped graphene as a heterogeneous electrocatalyst toward oxygen evolution. *Sci. Adv.* **4,** eaap7970 (2018).

17. Satoshi, Y., Koichiro, M. Computational modeling of the effect of varying aqueous solutions on $Ni(OH)_2$ precipitates. *AIP. Adv.* **8,** 025217 (2018).

18. Reina, C., Marian, J., Ortiz, M. Nanovoid nucleation by vacancy aggregation and vacancy-cluster coarsening in high purity metallic single crystals. *Phys. Rev. B.* **84,** 104117 (2011).

19. Ye, F., Liu, M., Tong, K., Li, Z., Che, H., Lei, M. Effects of uniaxial strain on stability and structural evolution of vacancy clusters in copper. *Comp. Mater. Sci.* **117,** 361-369 (2016).

20. Sun, S., Zhou, Y., Hu. B., Zhang, Q., Xu, Z. Ethylene glycol and ethanol oxidation on spinel Ni-Co oxides in alkaline. *J. Electron. Soc*. **163,** H99-H104 (2016**)**.

21. Corrigan, D. The catalysis of the oxygen evolution reaction by iron impurities in thin film nickel oxide electrodes. *J. Electron. Mater.* **134,** 377-384 (1987).

22. Trotochaud, L., Young, S. L., Ranney, J. K., Boettcher, S. W. Nickel-iron oxyhydroxide oxygen-evolution electrocatalysts: the role of intentional and incidental iron incorporation. *J. Am. Chem. Soc.* **136,** 6744 (2014).

23. Bediako, D., Kaiser, B., Surendranath, Y., Yano, J., Yachandra, V., Nocera, D. Structure-activity correlations in a nickel-borate oxygen evolution catalyst. *J. Am. Chem. Soc.* **134,** 6801-6809 (2012).

24. Su, X., Wang, Y., Zhou, J., Gu, S., Li, J., Zhang, S. Operando spectroscopic identification of active sites in NiFe prussian blue analogues as electrocatalysts: activation of oxygen atoms for oxygen evolution reaction. *J. Am. Chem. Soc.* **140,** 11286-11292 (2018).

25. Shin, H., Xiao, H., Goddard, W. In silico discover of new dopants for Fe-doped Ni oxyhydroxide ($Ni_{1-x}Fe_xOOH$) catalysts for oxygen evolution reaction. *J. Am. Chem. Soc.* **140,** 6745-6748 (2018).

26. Hunter, B. M., Gray. H. B., Muller, A. M. Earth-abundant heterogeneous water oxidation catalysts. *Chem. Rev.* **116,** 14120-14136 (2016).

27. Egerton, R. F., Cheng, S. C. Measurement of local thickness by electron energy-loss spectroscopy. *Ultramicroscopy* **21,** 231-244 (1987).

28. Tkalych, A. J., Zhuang, H. L., Carter, E. A. A density functional + *U* assessment of oxygen evolution reaction mechanism on β-NiOOH. *ACS. Catal*. **7,** 5329-5339 (2017).

29. Zaffran, J., Toroker, M. C.M., Understanding the oxygen evolution reaction on a two-dimensional NiO_2 catalyst. *ChemElectroChem*. **4,** 2764-2770 (2017).

30. Chen, H., Maytal, C. T., Water oxidation catalysis for NiOOH by a metropolis monte carlo algorithm. *J. Chem. Theory. Comput.* **14,** 2380-2385 (2018).

31. Li, Y. F., Selloni, A., Mechanism and activity of water oxidation on selected surfaces of pure and Fe-doped NiO_x. *ACS Catal.* **4,** 1148-1153 (2014).

Acknowledgments:

This work is financially supported by Singapore MOE Tier 1 R284000162114, Singapore NRF CRP funding R284000159281, and the Agency for Science, Technology and Research (A*STAR) of Singapore This research is also supported by A*STAR with a Grant No. of 152-70-00017 and computational resources were provided by National Supercomputing Centre Singapore (NSCC) and A*STAR Computational Resource Centre, Singapore (A*CRC). This project was partly supported by the Science and Engineering Research Council (SERC) of A*STAR of Singapore. Yonghua Du thanks the National Natural Science Foundation of China for support (11528510). The XAFCA beamline in SSLS, 1W1B, 4W2, 4B9A, 1W1A, 4B9B, 1W2A and 4B7B beamline of BSRF are gratefully acknowledged for providing beam time to support this project. The authors also thank the Center for Bioimaging Center of National University of Singapore for the use of facilities. The authors are grateful to Dr. Lirong Zheng, Xiaodong Chen, Yunpeng Liu, Yu Chen, Shengqi Chu, Guang Mo, Shuhu Liu, Zhihong Li and Ping Yang for assistance and helpful discussion in the synchrotron radiation characterization, and to Dr. Jia Zhang and Poh Chee Kok for contributions to the DFT calculations.

Author contributions:

X.P. Wang performed syntheses and electrochemical measurement of the samples. W.S.V. Lee and J. Wang and Z.B. Wang were responsible for the analysis of the electrochemical measurement results. H.J. Wu and S.J. Pennycook conducted STEM measurement. L.M. Liu and Y. Han carried out the low-dose TEM measurement. S.W. Chee and U. Mirsaidov were responsible for the liquid nitrogen low-dose TEM measurement. S.B. Xi, T.D. Hu, A. Borgna, J. Zhang and Y. H. Du were responsible for the *operando* XAFS measurement. J.O. Wang performed the Ni edge NEXAS measurement. Z.H. Wu carried out the synchrotron radiation XRD. Z.G. Yu and Y.W. Zhang conduct structure and OER simulation. J.M. Xue was responsible for the overall direction of the project and preparation of the manuscript.

Competing interest:

The authors declare no competing interests.